Inversion mechanism for the transport current in type-II superconductors

H. S. Ruiz,[1,*] C. López,[2] and A. Badía-Majós[1]

[1]*Departamento de Física de la Materia Condensada–I.C.M.A., Universidad de Zaragoza–C.S.I.C.,*
María de Luna 1, E-50018 Zaragoza, Spain
[2]*Departamento de Matemáticas, Universidad de Alcalá de Henares, E-28871 Alcalá de Henares, Spain*
(Received 26 August 2010; revised manuscript received 30 November 2010; published 18 January 2011)

The longitudinal transport problem (the current is applied parallel to some bias magnetic field) in type-II superconductors is analyzed theoretically. Based on analytical results for simplified configurations, and relying on numerical studies for general scenarios, it is shown that a remarkable inversion of the current flow in a surface layer may be predicted under a wide set of experimental conditions. Strongly inhomogeneous current density profiles, characterized by *enhanced* transport toward the center and reduced, or even negative, values at the periphery of the conductor, are expected when the physical mechanisms of flux depinning and consumption (via line cutting) are recalled. A number of striking collateral effects, such as local and global paramagnetic behavior, are predicted. Our geometrical description of the macroscopic material laws allows a pictorial interpretation of the physical phenomena underlying the transport backflow.

I. INTRODUCTION

Type-II superconductors under the action of a transport current and a longitudinal magnetic field may exhibit the counterintuitive phenomenon of negative resistance within a certain set of experimental conditions. This property, together with other intriguing phenomena such as the observation of paramagnetic moments and the *compression* of the transport current by the action of a parallel magnetic field, have been reported in the course of intense experimental and theoretical activities.[1–7] Most of these works were primarily concerned with the arrangement of the macroscopic current density **J** along the so-called nearly *force-free* trajectories. Recall that if **J** is *nearly parallel* to the magnetic induction **B**, moderate or weak pinning forces are needed for avoiding the detrimental flux-flow losses related to the drift of flux tubes driven by the magnetostatic force (**J** × **B** per unit volume). More specifically, negative voltages have been observed by different groups[2–4] when recording the current-voltage characteristics at specific locations on the surface of the sample (central region). In addition, the striking effect takes place within a definite interval of applied magnetic fields.

Within such a complex scenario, it was recognized early on that the observations could only be understood if new dissipation mechanisms, additional to the flux-flow phenomena, were considered. In particular, a prominent role happens to be played by the flux-line cutting (crossing and recombination) between adjacent tilted vortices.[5,8] Nevertheless, certain facts still remain to be fully understood. Thus, the challenging problem of inhomogeneous electric fields, even changing sign along the specimen surface, is hitherto open. On the other hand, important issues such as the consideration of irreversible effects related to the thresholds for flux depinning and cutting phenomena have not yet been reported. In this paper, we investigate the influence of such mechanisms on the establishment of critical negative-current structures within the superconducting state. This is to be considered as a step forward for gaining knowledge on the processes that operate just previous to the dissipation regime. Within such a physical scenario, the concentration of transport current toward the center of the sample, and the appearance of negative flow at the surface, will be predicted for a certain range of experimental conditions. To be specific, the application of different components of magnetic fields, their sequence, and characteristic values will be identified as relevant issues for the observation of negative currents.

The article is organized as follows. In Sec. II, we present the basic ideas about the theoretical approach used, that is, a general critical-state theory for type-II superconductors. An idealized slab-geometry arrangement is proposed, which is aimed to introduce the lowest level of complexity for our purposes. Then, in Sec. III, we perform a simplified analytical evaluation that allows us to capture the main underlying physical matters. In Sec. IV, a quasi-three-dimensional (quasi-3D) statement of the problem is solved by numerical means. This is needed for the consideration of inhomogeneities over the sample. A discussion about the scope of our investigation within the problem of negative currents is given in Sec. V.

II. CRITICAL-STATE APPROXIMATION

A. Classical Maxwell equation approach

The fundamental concept on which the critical-state theory relies is that, in many cases, the experimental conditions allow us to analyze the evolution of the system in the quasistationary regime. Thus, Ampère's law becomes $\nabla \times \mathbf{H} = \mathbf{J}$, and determines the distribution of supercurrents within the sample. When some external excitation (magnetic field and/or transport current) applies, the quasistationary evolution between successive equilibrium states is ruled by Faraday's law $\nabla \times \mathbf{E} = -\partial_t \mathbf{B}$. Here, the induced transient electric field is determined through an appropriate material relation $\mathbf{J}(\mathbf{E})$ and is used to update the profile of $\mathbf{J}$.

The material law encodes the mechanisms related to the breakdown of magnetostatic equilibrium as well as the dissipation modes operating in the transient from one state to the other. In this sense, there have been a number of theoretical proposals; from them (see Refs. 9, 10, and the citations

therein), we choose here the so-called *double critical-state model* (DCSM).[11] This approach allows for a straightforward connection between the mesoscopic flux depinning and cutting phenomena, and the field equations for the coarse-grained quantity **J**. On one hand, the model establishes the critical conditions $|\mathbf{J}_\perp| \leqslant J_{c\perp}$ and $|\mathbf{J}_\parallel| \leqslant J_{c\parallel}$ that relate to (i) the maximum pinning force on the vortex lines ($|\mathbf{J} \times \mathbf{B}| = J_\perp B \leqslant F_{\mathrm{p,max}}$) and (ii) the maximum variation of the tilt angle between vortices [notice that, from Eq. (7), one has $d\alpha \propto J_\parallel$].[12] On the other hand, as was thoroughly discussed in Ref. 10, the model also provides a rule that fixes the *trajectory* of the system through the dissipation excursion toward the new equilibrium state. Thus, corresponding to a very sharp transition from the superconducting state to some regime of high losses, one can argue that the final-state current density verifies a maximum projection law relative to the transient electric field, i.e., $\max(\mathbf{J} \cdot \hat{\mathbf{E}})$, which ensures the fastest return to equilibrium. Notice that, in one-dimensional (1D) situations (an infinite slab with a single-component applied magnetic field), this is trivially verified because by symmetry one has $\mathbf{J} \parallel \mathbf{E}$ and both perpendicular to **B**. In other words, one has $J_\perp = \mathrm{sgn}(E_\perp)J_{c\perp}$, with $E_\perp$ standing for the component of **E** along the direction $\mathbf{B} \times (\mathbf{J} \times \mathbf{B})$. In more general configurations, the maximum projection condition is not so simple because of the vectorial character of the problem. Thus, within the DCSM framework, the current density must transit from one state to another to fulfill the conditions $|\mathbf{J}_\perp| \leqslant J_{c\perp}$ and $|\mathbf{J}_\parallel| \leqslant J_{c\parallel}$. This may be expressed by a relation of the kind $\mathbf{J} \in \Delta$, with Δ having a rectangular section of size $2J_{c\parallel} \times 2J_{c\perp}$ in this case. In summary, the critical-state model in general 3D systems is posed by the system of equations

$$\nabla \times \mathbf{E} = -\partial_t \mathbf{B}; \quad \nabla \times \mathbf{H} = \mathbf{J} \ (\mathbf{B} = \mu_0 \mathbf{H}),$$
$$\nabla \cdot \mathbf{B} = 0; \quad \max \mathbf{J} \cdot \hat{\mathbf{E}} \ \text{with} \ \mathbf{J} \in \Delta. \tag{1}$$

Notice that, as equilibrium magnetization is usually neglected in the critical-state regime, $\mathbf{B} = \mu_0 \mathbf{H}$ is used.

The integration of the above system of equations supplemented by appropriate boundary conditions may be cumbersome, so an alternative formulation has been frequently used that is fully equivalent, and states the problem in a variational form. It is briefly explained in the forthcoming paragraphs.

B. Variational statement of the critical-state problem

From a mathematical point of view, the above problem is equivalent to the incremental minimization of the functional (field Lagrangian)

$$L[\mathbf{H}] \equiv \int_{\mathbf{R}^3} \left[\frac{\mu_0}{2}(\Delta\mathbf{H})^2 + \mathbf{p} \cdot (\nabla \times \mathbf{H} - \mathbf{J}) \right] d^3\mathbf{r}. \tag{2}$$

Here, one introduces the variable **p** as a *Lagrange multiplier* for enforcing Ampère's law. On the other hand, $\Delta\mathbf{H}$ represents the magnetic-field increment for the time step under consideration. Additionally, the algebraic condition $\mathbf{J} \in \Delta$ should be fulfilled in the minimization.

Notice that the Euler–Lagrange equations for this variational problem are

$$\partial_\mathbf{p}\mathcal{L} = 0 \Rightarrow \nabla \times \mathbf{H} - \mathbf{J},$$
$$\partial_\mathbf{H}\mathcal{L} - \partial^i\left(\frac{\partial\mathcal{L}}{\partial_i\mathbf{H}}\right) = 0 \Rightarrow \mu_0\Delta\mathbf{H} = -\nabla \times \mathbf{p}, \tag{3}$$

which identify $\mathbf{p} \simeq \mathbf{E}\Delta t$. From a mathematical point of view, **J** is no longer a variable but rather plays the role of a parameter to be adjusted in a direct algebraic minimization, i.e.,

$$\max(\hat{\mathbf{E}} \cdot \mathbf{J}) \Leftrightarrow \max(\mathbf{p} \cdot \mathbf{J}). \tag{4}$$

As one can see, both Ampère's and Faraday's laws are included in the variational formulation, as well as any domain Δ for the critical current material law. Technically, we emphasize that the shorter the path step, the better agreement with the standard Maxwell equation formulation. On the other hand, numerical methods for discrete constrained minimization can be used as an alternative to the integration methods for Maxwell's equations, which happens to be very convenient for dealing with 3D problems.

C. Application: 2D and 3D slab geometry

A further advantage of the methodology introduced above is that the constraint relation $\mathbf{J} \in \Delta$ allows a pictorial representation that provides a useful tool for the understanding of the current flow structures that arise in the longitudinal configurations. Notice that, in our case (DCSM conditions), Δ may be depicted by the cylindrical region in Fig. 1.

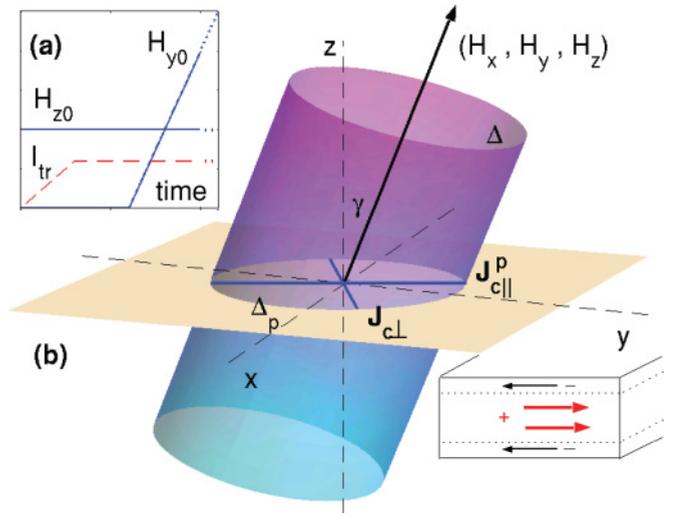Regarding the specific details about the mathematical technique for obtaining the numerical solution of Eq. (2),

FIG. 1. (Color online) (a)The magnetic process considered in this work. A magnetic field H_{z0} is applied perpendicular to the surface of a superconducting slab, which is later subjected to a transport current along the y axis and to an increasing field H_{y0}. (b) The critical current restriction is represented by a cylindrical region Δ around the local magnetic-field axis (length $2J_{c\parallel}$ and radius $J_{c\perp}$), Δ_p is the projection onto the slab (xy) plane, and γ is the angle between the field and the z axis. The lower inset depicts an element of the slab and the current backflow.

the interested reader is addressed to our Ref. 10. There, we analyzed a number of situations that are easily translated to the study within this work. Here, we will just mention that our proposal consists of transforming the volume integral over the whole space in (2) into a double integration over the sample's volume. Then, upon discretization, one solves for the distribution of the current in a proper set of circuits under the corresponding constraints for the components of **J** parallel and perpendicular to the local magnetic field. Thus, when one chooses the infinite slab geometry depicted in Fig. 1, such circuits are naturally defined by a collection of current layers within the xy plane, with each carrying a current density given by $[J_x(z_i), J_y(z_i)]$, with z_i the position of the layer. Notice that, because of the planar translational symmetry, a z component of **J** may be ruled out.

We emphasize that the slab geometry enables us to study the appearance of the focused physical phenomena with the least mathematical complication, i.e., this configuration allows us to clearly determine the mechanisms related to the negative currents. As a main fact, it will be established that, when building the parallel configuration, the response of the superconductor depends on the limitations for the current density given by the depinning threshold $J_{c\perp}$ on the orientation of the local magnetic field, and eventually on the flux-cutting restriction $J_{c\parallel}$. This is easily understood at a qualitative level just by glancing at Fig. 1. The critical current restriction is given by the region Δ_p, which is the intersection between the cylinder Δ and the xy plane where the current flows. For moderate values of the angle γ between the local magnetic field and the z axis, Δ_p is an ellipse of semiaxes $J_{c\perp}$ and $J_{c\parallel}^\mathrm{p}$ with

$$J_{c\parallel}^\mathrm{p} = J_{c\perp}/\cos\gamma = J_{c\perp}\sqrt{H_x^2 + H_y^2 + H_z^2}/H_z. \tag{5}$$

An increase of the in-plane magnetic-field component will result in a tilt of the cylinder by an increase of the angle γ. Note, in particular, that initially the maximum value of the in-plane parallel current density $J_{c\parallel}^\mathrm{p}$ grows with the angle γ, independent of $J_{c\parallel}$ (which is, thus, absent from the theory), until the maximum value $\sqrt{J_{c\perp}^2 + J_{c\parallel}^2}$ is reached. Then, the ellipse is truncated and eventually would be practically a rectangle of size $2J_{c\parallel} \times 2J_{c\perp}$ when $\gamma \to \pi/2$. Outstandingly, for large values of $\chi \equiv J_{c\parallel}/J_{c\perp}$ (long cylinders), the critical current along the parallel axis $J_{c\parallel}^\mathrm{p}$ increases more and more as the weight of H_{z0} decreases and, furthermore, this quantity is always beyond the individual values $J_{c\perp}$ and $J_{c\parallel}$.

III. SIMPLIFIED ANALYTICAL MODEL

We show here that some of the experimental features that will be obtained later in this paper from numerical calculations already may be predicted by a simplified analytical model. Let us consider the excitation process depicted in Fig. 1 for the particular case $H_{z0} = 0 \Rightarrow \gamma = \pi/2$ (the region Δ_p is a rectangle with axes defined by the directions parallel and perpendicular to **H**).

A. Governing equations

Ampère's law takes the following form for the infinite slab geometry considered in this work:

$$-\frac{dH_y}{dz} = J_x, \qquad \frac{dH_x}{dz} = J_y. \tag{6}$$

On the other hand, following the theory issued in Ref. 11, one can show that such expressions may be transformed into the polar form

$$-H\frac{d\alpha}{dz} = J_\parallel^\mathrm{p}, \qquad \frac{dH}{dz} = J_\perp^\mathrm{p} \tag{7}$$

with $H = \sqrt{H_x^2 + H_y^2}$ the modulus of the magnetic field vector and $\alpha = \mathrm{atan}(H_y/H_x)$ the angle between this vector and the x axis.

Now, the thresholds of flux depinning and cutting imply the in-plane conditions

$$|J_\parallel^\mathrm{p}| \leqslant J_{c\parallel}^\mathrm{p}(\gamma = \pi/2) = J_{c\parallel}, \qquad |J_\perp^\mathrm{p}| \leqslant J_{c\perp}. \tag{8}$$

It is apparent that, in general, Eq. (7) and the conditions in Eq. (8) would not straightforwardly lead to the solution of the problem. Typically, one should also use Faraday's law, either by explicit introduction of the related electric fields (as in Ref. 11), or by our variational statement. Nevertheless, in this case ($\gamma = \pi/2 \Rightarrow J_{c\parallel}^\mathrm{p} = J_{c\parallel}$), the resolution noticeably simplifies. In fact, for the situation considered, we will have a combination of the cases $J_\parallel^\mathrm{p} = 0, \pm J_{c\parallel}$ and $J_\perp^\mathrm{p} = 0, J_{c\perp}$ and the integration of Eq. (7) is straightforward. For further mathematical ease, we will also consider $J_{c\parallel}$ and $J_{c\perp}$ to be field-independent constants in this work.

The following normalization, based on the physical parameters that define the problem, will be used: $\vec{j} \equiv \mathbf{J}/J_{c\perp}$, $\mathbf{h} \equiv \mathbf{H}/J_{c\perp}a$, and $\mathbf{z} \equiv z/a$ (a is the half-thickness of the slab). The origin of coordinates will be taken at the center of the sample.

Following the notation introduced in Ref. 11, we will refer to different zones within the sample that are, in brief, macroscopic regions where well-defined dissipation mechanisms occur. Inserting our normalized units, there can be T zones, where only flux depinning (transport) occurs ($j_\parallel = 0, j_\perp = \pm 1$), C zones, where only flux cutting occurs ($j_\parallel = \pm\chi, j_\perp = 0$), and CT zones, where both transport and cutting occur ($j_\parallel = \pm\chi, j_\perp = \pm 1$). Finally, one will have O zones, where neither flux transport nor cutting take place ($j_\parallel = 0, j_\perp = 0$). Introducing these possibilities in Eqs. (7) and (8), one gets the following cases for the incremental behavior of the magnetic field in polar components:

$$dh = \begin{cases} 0 & (O,C), \\ \pm dz & (T,CT), \end{cases} \qquad d\alpha = \begin{cases} 0 & (O,T), \\ \pm(\chi/h)\,dz & (C,CT), \end{cases} \tag{9}$$

and all that remains for obtaining the penetration profiles is to solve successively (integrate) for h and α with the corresponding boundary conditions (evolutionary surface values h_0, α_0). The case selection has to be made according to Lenz's law. We note in passing that further specification related to the sign is usually included in the notation. Thus, a T_+ zone will exactly mean $dh = +dz$.
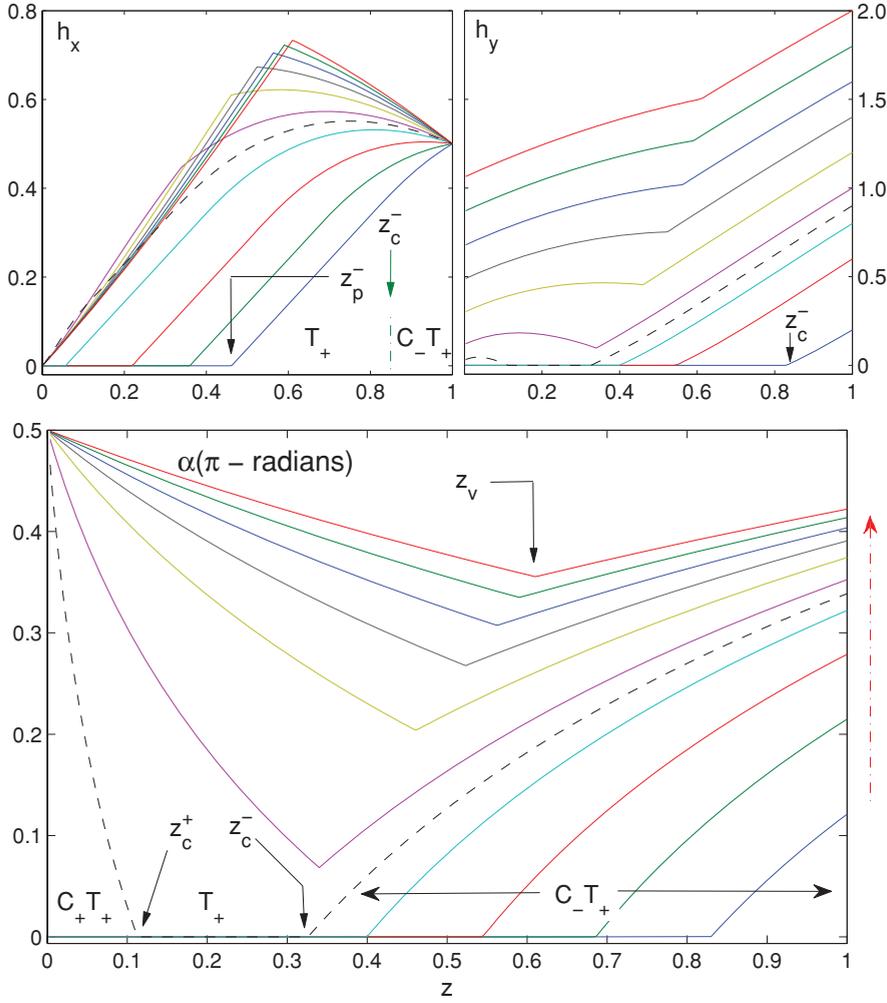
FIG. 2. (Color online) Penetration of the magnetic-field components and rotation angle in the longitudinal transport experiment ($H_{z0} = 0$) for a superconducting slab of thickness $2a$, as calculated from Eq. (7). The zone structure induced by increasing the field H_{y0} is marked upon some of the curves. The dashed line corresponds to the unstable regime (see text). Dimensionless units for h and z are defined in the text.

B. Magnetic process

1. Application of current

To start with, the application of the transport current along the y axis produces a T_+ zone

$$dh = dz, \quad d\alpha = 0,$$
$$\Downarrow \qquad\qquad (10)$$
$$h = h_{x0} + z - 1, \quad \alpha = 0,$$

which penetrates from the surface until the point where h equals 0, i.e., $z_{p0} = 1 - I_{tr}$. In our units, $z_{p0} = 0.5$ for $I_{tr} = h_{x0} = 0.5$. An O zone appears in the inner region $0 < z < z_{p0}$ as far as $I_{tr} < 1$.

2. Application of parallel field: initial steps

The above situation remains valid until h_{y0} is applied. Then, upon increasing h_{y0}, the flux-line rotation starts on the surface and the perturbation propagates toward the center in the form of a C_-T_+ zone defined by

$$dh = dz, \quad d\alpha = -\chi/h\, dz,$$
$$\Downarrow \qquad\qquad (11)$$
$$h = h_{x0} + z - 1, \quad \alpha = \alpha_0 + \chi \ln[1 + (z - 1)/h_0],$$

which covers the range $z_c^- < z < 1$, defined by $\alpha = 0 \rightarrow z_c^- = 1 + h_0[\exp(-\alpha_0/\chi) - 1]$. The former T_+ zone is pushed toward the center and occupies the interval $z_p^- < z < z_c^-$, with $z_p^- = 1 - h_0$. Finally, an O zone fills the core $0 < z < z_p^-$.

The upper panes of Fig. 2 sketch the above-described structure marked on the Cartesian components of the magnetic-field vector. The transition points between the different regimes are highlighted.

3. Application of parallel field: instability at the center

The $O/T_+/C_-T_+$ structure remains valid until the condition $z_p^- = 0 \Leftrightarrow h_0 = 1$ is reached, i.e., the modulus of **h** penetrates completely within the interval $0 < z < 1$. Then, the O zone disappears, and a T_+/C_-T_+ structure fills the sample. We emphasize that this configuration becomes unstable because of the boundary condition $h_x(z = 0) = 0$, which is dictated by the symmetry of j_y around the center. Thus, corresponding to the even behavior of $j_y(z)$, $h_x(z)$ must be an odd function. In physical terms, flux vortices penetrate from the surface with some orientation given by the components of the vector (h_x, h_y). Owing to the critical condition for the penetration of the field $dh/dz = 1$, as soon as the modulus reaches the center, flux rotation must take place there. This is needed for accommodating the vector to the

condition $\mathbf{h}(z = 0) = [0, h_y(z = 0)] = [0, h(z = 0)]$. On the other hand, as the angle variation is determined by the value of $J_{c\parallel}$, a jump is induced at the center, i.e., $\alpha(z = 0) \to \pi/2$, and the related instability may be visualized by a critical $C_+ T_+ / T_+ / C_- T_+$ profile (the dashed line in Fig. 2) in which the field angle decreases from its surface value α_0 to 0 in the $C_- T_+$ region, then keeps null within the T_+ zone, and suddenly increases to the value $\pi/2$ in the inner $C_+ T_+$ band defined by

$$dh = dz, \quad d\alpha = \chi / h \, dz,$$
$$\Downarrow \qquad (12)$$
$$h = h_{x0} + z - 1, \quad \alpha = \pi/2 - \chi \ln[1 + z/(h_0 - 1)].$$

In fact, a $C_+ T_+ / C_- T_+$ structure is stabilized with the intersection between regions at the point $[\alpha^{+,+}(z_v) = \alpha^{-,+}(z_v)]$ given by $z_v = 1 - h_0 + \sqrt{h_0(h_0 - 1)} \exp[(\pi/2 - \alpha_0)/\chi]$. Note that, upon further increasing h_{y0}, the point z_v follows the rule $z_v(h_{y0} \to \infty) \to (1 + h_{x0}/\chi)/2$. All these features have been marked in the lower pane of Fig. 2.

4. Physical phenomena

The previous results allow us to identify the following properties as h_{y0} is increased: (i) the appearance of a surface layer with negative-transport current density [mind the slope of h_x in Fig. 2 in view of Eq.(6)], and (ii) the applied magnetic-field *reentry* as related to the inner $C_+ T_+$ zone. These features will be confirmed in the forthcoming paragraphs, where the numerical solution of the problem is presented. Additionally, we will show that the inclusion of a third component of the magnetic field ($h_{z0} \neq 0$ in what follows) allows us to unveil further details reported in the literature. In particular, the

occurrence of the negative-current phenomenon at specific locations on the surface of the sample and for a given range of applied magnetic field will be understood within the three-dimensional scenario.

IV. NUMERICAL RESULTS

Next, we detail the results obtained numerically for different material laws as related to the selection of the critical current region Δ. We restrict the plots to the limiting cases $j_{c\parallel} \to \infty$ and $j_{c\parallel} = 1$ (infinite and unit aspect ratio, or also named after T and CT states for obvious reasons). The information of interest for intermediate values is straightforwardly interpolated.

From a technical side, we must point out that when minimizing L [see Eq.(2)], a slightly smoothed version of the cylindrical region Δ has been considered by means of a *superelliptic* relation[13] given by

$$j_\perp^{2n} + (j_\parallel/\chi)^{2n} \leqslant 1 \qquad (13)$$

with $n = 4$. This statement performs with a high stability from a numerical point of view. Figures 3 and 4 display the main features obtained for the longitudinal transport experiment when the third component of the magnetic field (h_{z0}) is incorporated. First, we will analyze the properties of the field [$\mathbf{h}(z)$] and current density [$\vec{j}(z)$] profiles for a longitudinal configuration built in the fashion described in Fig. 1. Figure 3 contains the behavior of these quantities as h_{y0} (the applied parallel field) is increased, subsequent to the application of the transport current. This is done for a low and a high value of the perpendicular magnetic field h_{z0}. For the meaning of low and high, recall that, along with this work,
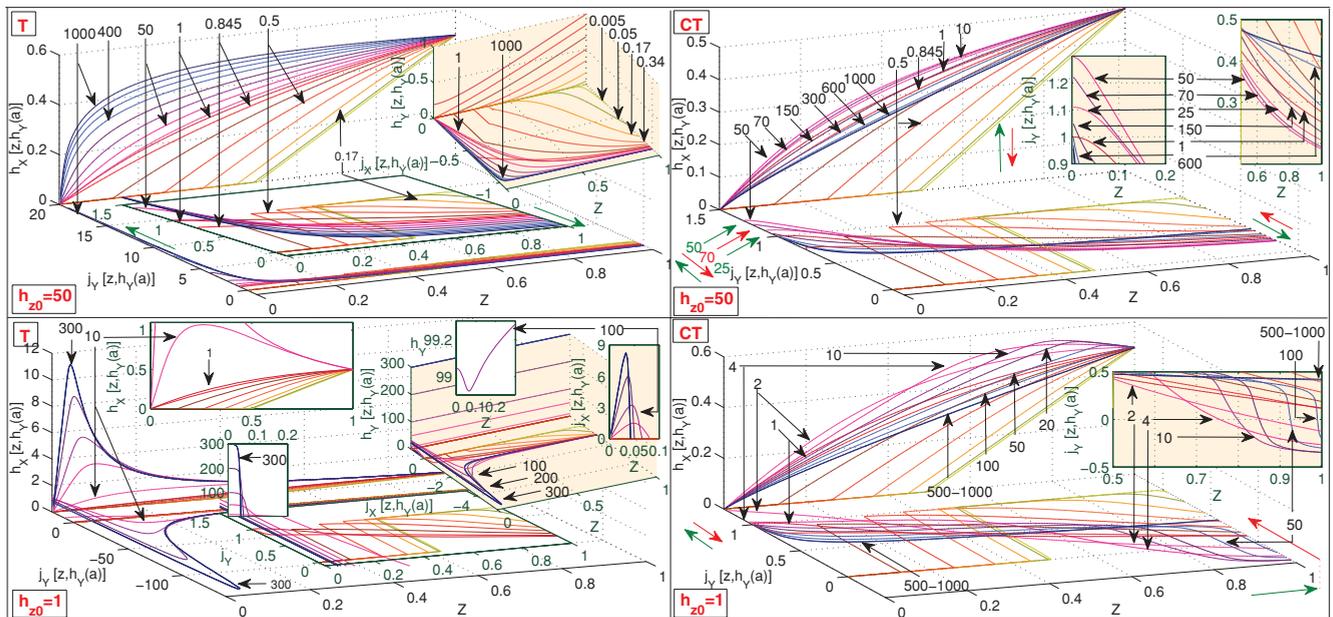

FIG. 3. (Color online) Profiles of the magnetic-field components $h_x[z, h_y(a)]$ and $h_y[z, h_y(a)]$, including their corresponding current density profiles $j_y[z, h_y(a)]$ and $j_x[z, h_y(a)]$ for the T-state model (left) and the superelliptic CT model (right). The magnetic dynamics for high (top) and low (bottom) perpendicular magnetic field h_{z0} is shown. Different scales are used to visualize the intricate behavior and to emphasize the appearance of negative currents at the surface. The curves are labeled according to the longitudinal magnetic-field component at the surface of the slab $h_y(a) \equiv h_{y0}$.

the units are relative to the characteristic penetration field value $H^* = J_{c\perp}a$.

A. Field and current density penetration profiles

The curves in Fig. 3 provide a basic mapping of the physical conditions in which negative currents occur. For completeness and for quantitative purposes, we have included both the field and current density profiles. Nevertheless, they are related by Ampère's law [Eq. (6)] as one can easily check at a qualitative level, i.e., in the slab geometry, $J_{x,y}$ is the slope of $H_{y,x}$, respectively.

Recall that negative values of the transport current density j_y are not noticeable for either the T or CT states when h_{z0} is high ($h_{z0} \gtrsim 50$) until extreme values of the longitudinal field ($h_{y0} \gtrsim 1000$) are reached. On the contrary, one can easily find negative current flow for both cases when $h_{z0} = 1$. If $j_\parallel$ is unbounded (T states), the $j_y(z)$ structure becomes rather inhomogeneous as h_{y0} increases and takes the form of a highly positive layer in the center *shielded* by a prominent negative region. When $j_\parallel$ is bounded (CT states), one observes a negative layer at the surface, which eventually disappears when h_{y0} increases more and more ($h_{y0} > 50$).

Some fine structure details are also to be noticed: (i) For the magnetic process under consideration, the *partial penetration regime* in which the flux-free core progressively shrinks to zero (curves labeled $h_{y0} = 0.005, \ldots, 0.845$) is practically independent of the critical current model (region) used; (ii) the peaked structure of $j_y(z)$ for the T states at $h_{z0} = 1$ (curves labeled $h_{y0} = 10, \ldots, 300$) is accompanied by a similar behavior in $j_x(z)$ that relates to a subtle magnetic-field reentry phenomenon in $h_y(z)$ as outlined in the plot; and

(iii) the negative values of $j_y(z)$ are obtained for smaller and smaller h_{y0} as h_{z0} also decreases. In fact, negative values can happen even for the partial penetration regime ($h_{y0} \lesssim 0.845$) when h_{z0} tends to 0, in accordance with the analytical model presented before (Sec. III).

B. Experimental quantities

For a closer connection with real experiments, we have also calculated the sample's magnetic moment **M** as a function of the longitudinal field. The fingerprints of negative-current flow will be identified. Figure 4 displays the magnetization process of the slab as a function of the applied longitudinal-field amplitude h_{y0}. **M** (in units of $J_{c\perp}a^2$), as well as the transport current density at the center $j_y(0)$ and at the surface $j_y(a)$, are displayed.

Several features are to be identified:

(i) Unlimited growth of $M_x(h_{y0})$ and $j_y(0)$ occur for the T states, in which $j_\parallel$ is unbounded. On the other hand, the appearance of a peak structure in $M_x(h_{y0})$ correlates with a maximum value of the transport current density at the center of the slab for the CT states. The obtained maximum value $j_y^{\max}(0) = 1.2968$ corresponds to the optimal orientation of the region Δ, in which the biggest distance within the superelliptic hypothesis is reached. Such a situation is sketched in Fig. 5 and one may check the numeric result from the expression

$$\max j_{c\parallel}^p = (1 + \chi^{2n/(n-1)})^{(n-1)/2n} \tag{14}$$

when the choices $\chi = 1$ and $n = 4$ are used. This formula is obtained from Eq. (13) after straightforward calculations. Notice that, as a limiting case, it produces the expected value
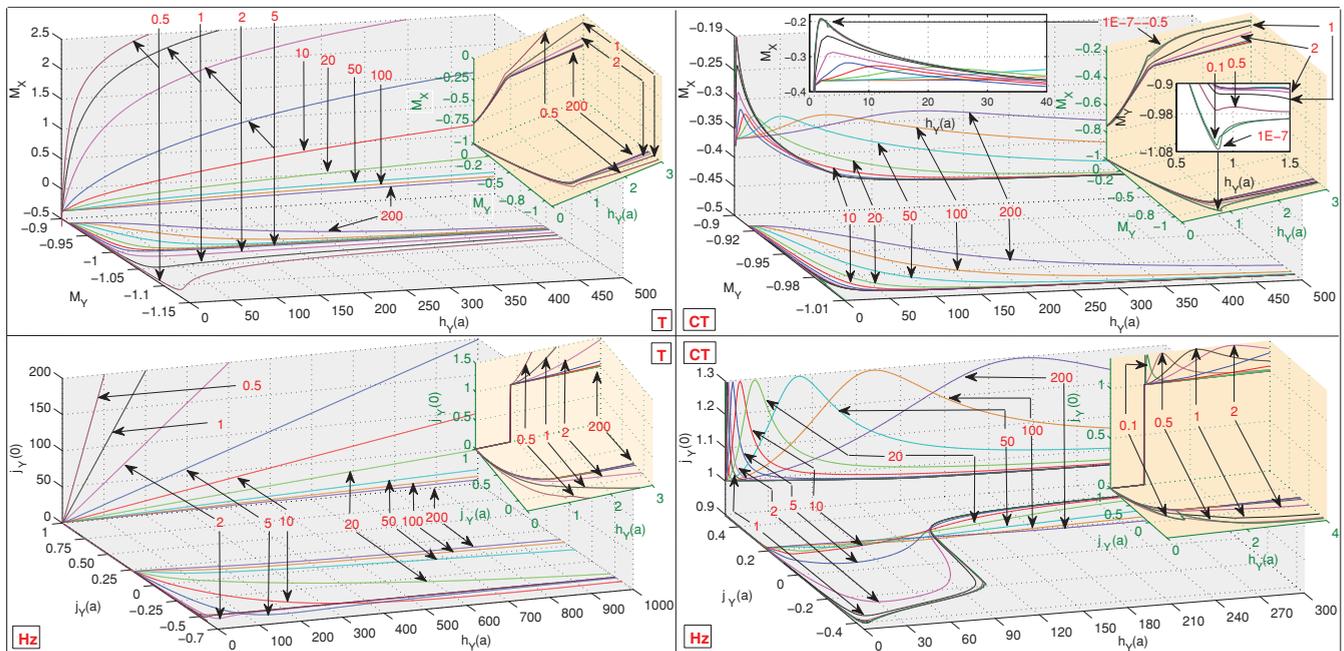

FIG. 4. (Color online) Top: Components of the magnetic moment of the slab as a function of the applied longitudinal magnetic field $h_{y0} = h_y(a)$ for the T-state model (left) and the superelliptic CT model (right) with different values of the perpendicular magnetic-field component h_{z0} as labeled by arrows on each curve. The magnetization dynamics at low fields h_{y0} is shown in the 3D insets. Notice the different scales. Bottom: The corresponding evolution of the transport current j_y at ($z = 0$) and ($z = a$).
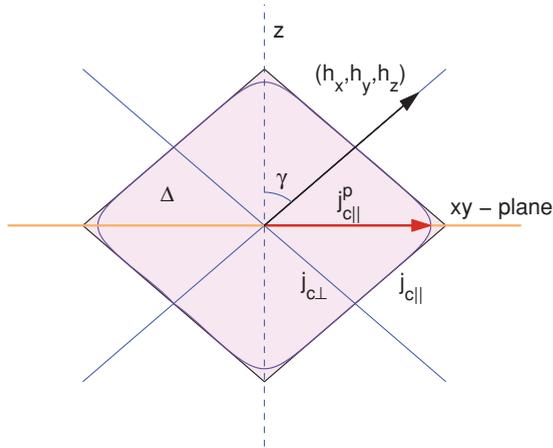
FIG. 5. (Color online) Side view of the critical current region Δ rotated by an angle γ that produces a maximal parallel current at the xy plane (this plot is a specific longitudinal section of Fig. 1). The precise orientation takes place for a definite value of the applied magnetic field h_{y0}. The superelliptical region considered in this work has been plotted together with the strictly CT model.

$2^{1/2}$ for the diagonal of a perfect square [i.e., $n \to \infty$ in Eq.(13)].

(ii) For the unbounded case, in the low h_{z0} regime, the negative-current density at the surfaces stabilizes toward the value $j_y(a) = -0.5$.

(iii) For the bounded case, and moderate or low h_{z0}, the transport current at the surface stabilizes toward the value $j_y(a) = 0.422$ whether or not it has been negative along the ramp of the applied longitudinal field.

(iv) As a general rule, the smaller the value of h_{z0}, the sooner the negative transport current is found. In the CT case, this also increases the range of longitudinal field for which negative values are observed.

V. DISCUSSION

Within the previous sections, we have displayed a number of cases in which negative transport layers are predicted for type-II superconductors if the longitudinal-field configuration ($\mathbf{J} \parallel \mathbf{B}$) is induced by some external process. Our theoretical investigations allow us to identify the following relevant aspects for the appearance of such phenomenon.

(i) The physical mechanisms of *flux cutting and depinning*, that may be modeled by the thresholds for the components of $\mathbf{J}$ parallel and perpendicular to the local magnetic field. In this sense, we have shown that negative currents are much more easily observed for materials in which $J_{c\parallel}$ and $J_{c\perp}$ are independent and $J_{c\parallel} \gg J_{c\perp}$. On the other hand, additional calculations (not displayed) imply that an alternative ansatz as the isotropic model ($J_\parallel^2 + J_\perp^2 \leqslant J_c^2$, i.e., the difference between the mechanisms responsible for the thresholds $J_{c\parallel}$ and $J_{c\perp}$ are not relevant and the region Δ is a circle) can not predict such behavior. However, if some interaction is allowed between the cutting and depinning thresholds [moderately smoothed $J_\perp(J_\parallel)$ relation, i.e., the region Δ is a superellipsoid], the negative-current flow will occur for some range of conditions.

(ii) The *sequence in which the external excitation components are applied* to the superconductor. Thus, as one could expect from the idea that, in the critical state, all changes proceed from the surface toward the center of the sample, negative-current structures are enhanced when the applied magnetic field is applied after originally building a subcritical transport profile. Recall that in the situations depicted in Fig. 3, the initial current flow is compressed more and more, even until compensating negative values are needed at the surface for maintaining the biased transport current. Along these lines, we should comment that, when simulating experiments in which the transport current is applied subsequent to the field, our theory does not predict negative flow values at all. On the contrary, in such cases, what one gets is a *compression* of the original field penetration profile until the increasing transport current leads to dissipation.

Additional physical considerations can be done so as to cover the full experimental scenario. In particular, although our analysis has been performed within the infinite slab geometry, one can straightforwardly argue about the extrapolation to real experiments. Thus, the inclusion of the third component of the magnetic field H_{z0} relates to the last relevant aspect.

(iii) The importance of the *finite-size effects*. Notice that, from our numerical calculations, one can predict that negative currents should be more prominent in those regions of the sample where the component of $\mathbf{H}$ perpendicular to the current layers is less important. This will occur at the central region of the sample's lateral surface, where end effects are minimal. Thus, considering that a real sample in a longitudinal configuration typically will be a rod with field and transport along the axis, the above idea is straightforwardly shown by plotting the penetration of an axial field in a finite cylinder. This has been done in Fig. 6. The plot shows the distortion
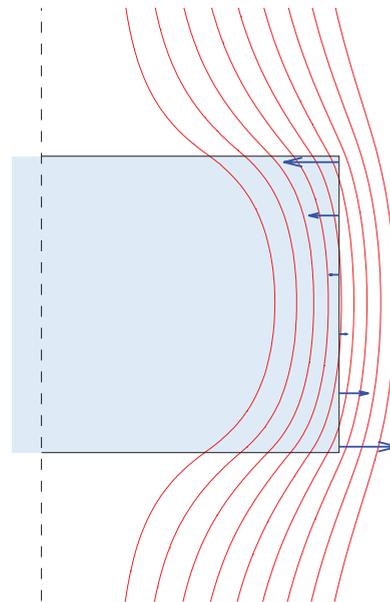

FIG. 6. (Color online) Penetration of a magnetic field parallel to the axis of a finite superconducting cylinder (a half-longitudinal section is shown for symmetry reasons). The component of the magnetic field perpendicular to the lateral surface is visualized by a set of arrows with normalized lengths. The dashed line represents the symmetry axis.

of the magnetic field, shielded by the induced supercurrents. Just for visual purposes, we have superimposed the horizontal component of the magnetic field, along the lateral side of the cylinder. It is apparent that the normal component of **H** will be enhanced close to the bases and tend to zero at the central region. Thus, inhomogeneous surface current densities with negative flow at the mid part should be expected.

VI. CONCLUDING REMARKS

In this paper, we have shown that the counterintuitive effect of negative-current flow in type-II superconductors may be predicted and quantified by means of the critical-state theory. For restricted situations (infinite slab geometry and fields parallel to the surface), the prediction may even be made within a simplified analytical model. Three-dimensional effects may be incorporated by numerical methods when a third component of the magnetic field, perpendicular to the surface of the slab, is considered. The analysis of this situation has allowed us to conclude that negative transport is enhanced for superconductors in which the flux-cutting barrier is much above the depinning value, and at those regions of the sample where the magnetic field is basically parallel to the surface (central part in cylinder geometry).

Extensions of this work are planned along two lines: (i) the actual evaluation of the longitudinal problem in finite length samples (field and transport along the axis of a rod), and (ii) the extrapolation of the current density profiles beyond the critical-state threshold, so as to include the dissipation effects.

*hsruizr@unizar.es

[1] A. M. Campbell and J. E. Evetts, Adv. Phys. **21**, 199 (1972), and references therein; T. Ezaki, K. Yamafuji, and F. Irie, J. Phys. Soc. Jpn. **40**, 1271 (1976).

[2] D. G. Walmsley, J. Phys. F **2**, 510 (1971); D. G. Walmsley and W. E. Timms, *ibid.* **7**, 2373 (1977).

[3] J. R. Cave and J. E. Evetts, Philos. Mag. B **37**, 111 (1978).

[4] T. Matsushita, A. Shimogawa, and M. Asano, Phys. C (Amsterdam) **298**, 115 (1998).

[5] J. R. Clem, J. Low Temp. Phys. **38**, 353 (1980); E. H. Brandt, *ibid.* **39**, 41 (1980).

[6] I. F. Voloshin, N. V. Il'in, N. M. Makarov, L. M. Fisher, and V. A. Yampol'skii, JEPT Lett. **53**, 115 (1991) [Pis'ma Zh. Eksp. Teor. Fiz. **53**, 109 (1991)].

[7] L. M. Fisher, A. V. Kalinov, S. E. Savel'ev, I. F. Voloshin, and V. A. Yampol'skii, Solid State Commun. **103**, 313 (1997).

[8] M. A. R. LeBlanc, S. Celebi, S. X. Wang, and V. Plechacek, Phys. Rev. Lett. **71**, 3367 (1993).

[9] A. Badía and C. López, Phys. Rev. Lett. **87**, 127004 (2001).

[10] A. Badía-Majós, C. López, and H. S. Ruiz, Phys. Rev. B **80**, 144509 (2009).

[11] J. R. Clem and A. Pérez-González, Phys. Rev. B **30**, 5041 (1984).

[12] E. H. Brandt, J. R. Clem, and D. G. Walmsley, J. Low Temp. Phys. **37**, 43 (1979); J. R. Clem, Phys. Rev. B **26**, 2463 (1982).

[13] Recall that the relation $(x/a)^{2n} + (y/b)^{2n} = 1$ represents a family of closed curves (superellipses) with semiaxes a and b, ranging from an ellipse to a rectangle as n follows the sequence $n = 1, 2, 3, \ldots, \infty$. This was exploited in Ref. 10 for comparing different critical-state material laws.